



ABWR

Students: Simran Mandal and Nicolas Becquet

Course: SH2702

Spring term 2023

Contents

Introduction	1
1 Design features, operating parameters and safety of ABWR	3
1.1 Increased plant output and turbine design	3
1.2 Improved core and fuel design	3
1.3 Description of the primary system	4
1.4 Operating characteristics	10
1.5 Safety	13
1.6 Summary	14
2 Calculation of selected core parameters	15
2.1 Power Distribution	15
2.2 Enthalpy distribution	16
2.3 Pressure Drop	18
2.4 Coolant temperature distribution	21
2.5 Flow characteristics of the core	22
3 Calculation of CHF margins in a hot channel	23
3.1 Power distribution	24
3.2 Enthalpy	24
3.3 Pressure Drop	26
3.4 Coolant temperature distribution	27
3.5 Dryout type CHF calculation	28
4 Calculation of the maximum cladding and fuel pellet temperature	31
4.1 Coolant to clad interface	32
4.2 Gas to fuel interface	34
4.3 Fuel to fuel center interface	34
4.4 Radial distribution of temperature in gas layer and cladding	36
4.5 Conclusion and temperature field in the rod	38
A Appendices	41
References	43

Introduction

The ABWR is known around the world as the first generation III nuclear reactor to have been fully developed, with a first reactor commissioned in 1996 in the Kashiwazaki-Kariwa nuclear power plant. This design has been developed by General Electric in collaboration with Toshiba, Hitachi, and other international partners. It incorporates several innovations that improve the efficiency of the reactor, reduce the risk of accidents, and lower the overall cost of electricity generation. One of the biggest selling points of this reactor is that it was built, from start to finish in just four years. The capital cost of building the reactor was about \$ 1600/kW, which make it very competitive with other sources of power generation.

A new era of secure, affordable, and ecologically responsible nuclear electricity is introduced with the successful design, licensing, construction, and operation of the ABWR nuclear power station.

In this report, we will begin by describing the main characteristics of the ABWR reactor : its technical specificities, its operation principles and its main safety features. Then, we will focus on the core of the reactor and present the results of some simulations that we made on Python and which allowed us to describe parameters of the coolant and the fuel rods such as pressure, temperature, void fraction, ...

Abbreviations

ABWR: Advanced Boiling Water Reactor
ADS : Automatic Depressurization System
BWR : Boiling Water Reactor
CRD : Control Rod Drive
CRGT : Control Rod Guide Tube
FIV : Flow Induced Vibration
FMCRD : Fine Motion Control Rod Drive
HCU : Hydraulic Control Unit
LOCA : Loss of Coolant Accident
M-G : Motor-Generator
MSIV : Main Steam Isolation Valve
MSL : Main Steam Line
PCV : Primary Containment Vessel
R&D : Research and Development
RIN : Reactor INternals
RIP : Reactor Internal Pump
RPV : Reactor Pressure Vessel
RRS : Reactor Recirculation System
S-FMCRD : Seal-less Fine Motion Control Rod Drive
SRV : Safety Relief Valve
T&D : Tests and Development

1. Design features, operating parameters and safety of ABWR

BWR has evolved in two major areas: the reactor system and containment design. This evolution was the result of design improvements and the insights acquired from operating reactors and testing programs. The process of continuing BWR simplification has led us to the total elimination of external recirculation loops and internal jet pumps, followed by the use of internal recirculation pumps in the ABWR.

The primary goals of designing the ABWR plant were to:

- Improve plant operability, maneuverability, and daily load following capability.
- Improve plant safety and reliability.
- Increase plant availability and capacity factor.
- Reduce occupational radiation exposure.
- Reduce plant capital and operating costs.

1.1 Increased plant output and turbine design

The ABWR plant is designed to have a rated thermal output of 3,926 MW and an electrical output of more than 1,350MWe. The turbine design incorporates a 52-inch last stage bucket design to improve plant efficiency, performance, and economy. Combined moisture separator/reheaters remove moisture from the steam and reheat it in two stages. In order to increase plant output while lowering costs, the design incorporates both high pressure and low pressure pumped-up drains. Rather than returning the heater drains to the condenser, the pumped-up drain system utilizes this waste heat and injects it back into the feedwater ahead of the heaters.

This concept increased generator output by roughly 5 MWe, reduced condensate polisher capacity, and reduced the size requirements for both the high and low pressure heater areas. The overall design has made the best use of design improvements to maximize plant output while lowering costs.

1.2 Improved core and fuel design

The ABWR core and fuel design aimed to improve the plant's operating efficiency, operability, and fuel economy. The performance objectives were met by using PCI-resistant (barrier) fuel, axially zoned reactivity of the fuel, control cell core design, and increased core flow capability. By using minimum shuffle fuel loading schemes, it was possible to reduce refueling times. Meanwhile, increased fuel burnup to higher values enables longer continuous operating cycles and is projected to result in lower fuel cycle costs.



The axially zoned reactivity fuel, which has higher enrichment and less neutron absorber content in the upper half of the fuel rods, allows for uniform axial power distribution throughout the operating cycle. This feature ensures a higher thermal margin, which results in improved fuel integrity, plant capacity factor, and operational

flexibility when combined with the other core design features. The shallow control rods that control the axial power shape are eliminated by the axially zoned reactivity fuel, and the control rods are only used to control reactivity. This helps to extend the life of the control rods because many of them can now be fully withdrawn from the core while operating at full power.

The control cell core concept, which has been successfully applied to many of the most recent operating plants, is used in the core design. Except for those in specially selected control cells, all control blades in this design are fully withdrawn throughout an operating cycle. Each control cell is made up of four depleted fuel bundles that surround a control blade. Only these rods move to compensate for reactivity in each control cell, while all other rods remain fully withdrawn. This reduces the operator's control rod manipulation tasks and focuses him solely on control cell rods during the cycle to compensate for reactivity or power distribution shaping. This design also increases capacity factor because the control cell eliminates the need for rod sequence exchanges, which were required in previous plants. The use of axially zoned fuel allows for flat hot excess reactivity, which reduces rod adjustment during the cycle.

With flow rate adjustment and no control blade movement, daily load following from 100% to 70% to 100% power (in a 14-1-8-1 h cycle) is simple. Load following of 100%-50%-100% is easily performed for both maximum use of the core flow and slight control blade adjustment. Furthermore, the excess flow capacity enables spectral shift operation to provide additional burnup with all rods out, increasing operational flexibility, extending operation time, and lowering fuel cycle costs.

1.3 Description of the primary system

The primary system's main jobs include transporting the steam produced in the core to the turbine system and performing safety tasks like keeping the primary containment vessel (PCV) isolated from the radioactive materials during an accident and preventing overpressure during pressurization transients.

The primary system of ABWR mainly consists of reactor pressure vessel and reactor internals (RPV/RIN) system, reactor recirculation system (RRS), steam separation system, main steam line (MSL) system, and control rod drive (CRD) system and excludes the core. Figure (1.1) provides a visual representation of the ABWR primary system.

The turbine system's feedwater is injected into the reactor pressure vessel (RPV) via feedwater spargers. The feedwater combines with the water returning from the separators and dryers and flows downward through the downcomer, an annular region between the reactor vessel and the core shroud that forms the recirculation flow.

Recirculation pumps, which consist of ten reactor internal pumps (RIPs) installed in the bottom of the RPV, supply the driving force for the recirculation flow. The pumped water enters the bottom plenum where it reverses flow to upward. Water enters the core through the input orifices and flows along and outside of the control rod guide tubes (CRGTs), which alter the flow rate for the fuel channels.

The water in the core acts as a moderator and a coolant, receiving heat pri-

marily from the fuel rods and vaporizing it. approximately 15% quality at the core's exit.

The coolant forms a two-phase flow of



The mixture of steam and liquid water flows through the standpipes and into the steam separators, where centrifugal force separates the water. The steam with very small droplets passes through the dryer assemblies, removing the majority of the remaining droplets.

The steam from the RPV is routed to the turbine system via four main steam lines. The residual water from the separators and dryer assemblies enters the downcomer. The power level of the reactor is controlled by the control rods. Control rod drive (CRD) mechanisms insert and withdraw them vertically from the core. Bottom-entry CRDs are mounted on the reactor vessel's bottom head. When control rods are withdrawn, they are inside the CRGTs below the core.

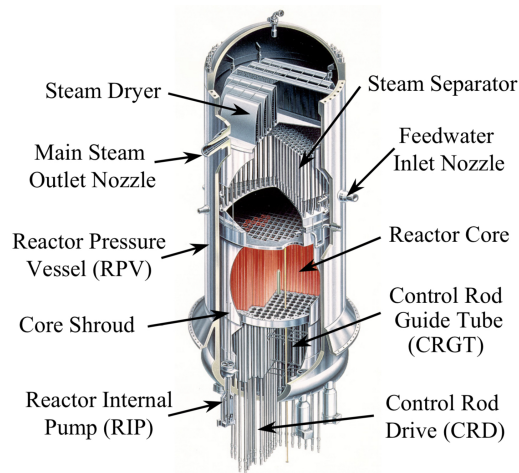


Figure 1.1: ABWR primary system

1.3.1 RPV/RIN system

The RPV system, which is located in the center of the PCV, is made up of the main body of the RPV as well as its appurtenances, supports, and insulation. During plant operation, it houses the reactor core and serves as a radioactive material barrier.

The RPV is a vertical, cylindrical welded vessel with a detachable top head. The number of welds in the RPV is reduced by using large forged rings. The cylindrical shell, flange, bottom head, RIP casings, penetrations, brackets, and nozzles comprise the RPV's main body.

In the event of a failure of the reactor coolant pressure boundary associated with the CRD housing weld, the RPV system restrains the CRDs to prevent ejection of the control rod connected with the CRD. Each RIP also has a restraint system to prevent it from becoming a missile in the event of a failure of the reactor coolant pressure boundary associated with the RIP casing weld.

The reactor vessel is supported on the reactor pressure vessel pedestal by a reactor vessel support skirt. Anchor bolts extend from the pedestal through the skirt's flange. To resist horizontal loads, RPV stabilizers are installed in the upper portion of the RPV.

RPV system's major reactor internal components are core support structures and other reactor internals.

The shroud, shroud support, core plate, top guide, fuel support, and CRGTs are examples of core support structures. The shroud support is made up of a short

vertical cylindrical shell, a horizontal annular pump deck plate that serves as a partition between the RIP suction and discharge, and vertical support legs.

Feedwater spargers, shutdown cooling, and low pressure core flooders spargers for the residual heat removal system, as well as high pressure core flooders spargers and couplings, are among the other reactor internals.



Table (?) summarizes the major plant specifications as well as the primary system specifications of ABWR.

1.3.2 Reactor recirculation system (RRS)

The RRS circulates the required amount of coolant through the core and controls reactivity by varying the void fraction in the core via the recirculation flow rate.

The main feature of the ABWR RRS is the use of reactor internal pumps (PIRs), which eliminates the need for traditional external loops such as external recirculation pumps, large diameter pipes, and internal jet pumps. The use of RIPs simplifies the system and contributes to design improvements in the following ways:

1. Increased safety due to the absence of large diameter pipes below the core top level,
2. Compact PCV and reactor building,
3. Power reduction for the recirculation system,
4. Reducing radiation exposure, and
5. Shortening the inspection period and reducing in-service inspections.

"Test before use" was the guiding principle for incorporating new components into the ABWR. For that more than 20 programs, including those for RIP, were carried out as Joint Study Programs by Japanese BWR utilities and three BWR manufacturers for testing and development (T&D). Furthermore, the Japanese government funded a comprehensive and full-scale verification test of the RIP system at Nuclear Power Engineering Corporation (NUPEC).

The reactor coolant is forced through the lower plenum, up through the reactor core, steam separators, and back down the downcomer annulus by ten RIPs mounted in the bottom of the RPV.

To control the core reactivity through the void fraction in the core, the recirculation flow rate is variable over a "flow window" ranging from 90% to 111% of the rated flow rate. Each RIP's rotating speed is controlled by an adjustable speed drive (ASD).



Six out of ten ASDs are powered by motor-generator (M-G) sets. The M-G set prevents boiling transition of fuel rods, a sudden deterioration in boiling heat transfer caused by a mismatch of heat flux and coolant flow rate, resulting in cladding temperature excursion, in the event of all RIP trip events.

1.3.3 Steam separation system

The steam separation system separates the steam from the steam-water mixture and dries the steam sufficiently to supply the turbine system.

Steam separators and steam dryers make up the steam separation system. The former uses centrifugal force to separate liquid droplets and steam, while the latter uses waved vanes to reduce the moisture in the steam. The steam separators are welded to the tops of the shroud head's standpipes, and the steam dryer assemblies are mounted above the steam separators. Figure (1.2) depicts a vertical cross sectional view of a steam separator.

At the inlet, a swirler is installed. The mixture rising through the standpipe collides with the vanes, which spin the mixture and generate swirl flow, separating liquid droplets from steam as it flows upward in the three-stage barrel. Steam exits the separator at the top and enters the plenum beneath the dryers. Water film forms on the barrel wall gradually and is removed by pick-off rings before flowing through discharge paths into the pool surrounding the separators.

The steam dryer assemblies are installed on top of the steam separators. Steam from the separators flows up and out of the drying vanes. Moisture is removed by the vanes and drains into the pool via troughs.

Pressure loss is caused by steam separators, which are part of the recirculation system. Lower steam separator pressure loss is beneficial because it reduces the required pump head and pump power, resulting in an increase in the plant's net electric power output.

Many design parameters were changed to reduce pressure loss while maintaining separation performance through analysis. The improved steam separator is expected to have a pressure loss that is more than 30% lower than the conventional one.

1.3.4 Main steam line (MSL) system

During normal operation, the primary function of MSL system is to direct steam from the RPV to the turbine system. Another important function of the MSL system is to prevent primary system overpressure during plant transients that result in high system pressure as well as to keep radioactive materials inside the PCV during MSL break accident conditions.

The RPV emits steam through four nozzles. The venturi-type flow element built into the nozzles of each MSL measures the steam flow rate. The flow element also has a safety function that limits the coolant blowdown rate from the RPV in the event of an MSL break.

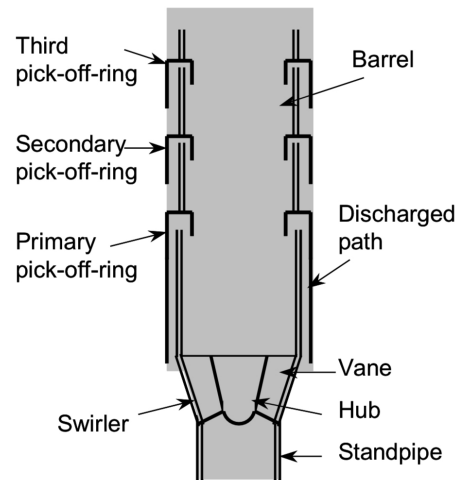


Figure 1.2: Steam separator structure

To protect the reactor primary system from overpressure, 18 safety/relief valves (SRVs) are installed on the MSLs between the RPV and the inboard MSIV in the ABWR.

The valves are intended to operate in both a safety and a relief mode. Each SRV is connected to a quencher in the suppression pool, where the discharged steam is condensed.

The total capacity or number of SRVs is determined by analyzing the most severe pressurization transients, such as turbine trip or complete MSIV closure. During transient events, it is intended to limit the peak pressure of the primary pressure boundary component to less than 110% of the design pressure.



Eight valves are chosen from a total of eighteen SRVs to be designed with the automatic depressurization system (ADS) function for small break LOCAs.

Each of the four MSLs has two main steam isolation valves (MSIVs), one inboard and one outboard of PCV penetration. During an MSL break accident, the MSIV has a safety function that isolates radioactive materials inside the PCV.

The MSIV is a Y-pattern globe valve with a spring-loaded, pneumatic piston. During normal operation, the Y-pattern configuration allows for a low-pressure loss.

1.3.5 Control rod drive (CRD) system

The CRD system is responsible for inserting and withdrawing the control rod to the designated position to control the core reactivity during normal operation, and to rapidly insert the control rod in response to a manual or automatic scram signal. The fine motion control rod drive (FMCRD) mechanisms, the hydraulic control unit (HCU) assemblies, and the control rod drive hydraulic subsystem encompass the ABWR's CRD system.

The FMCRD is designed to provide electric-motor-driven positioning for normal control rod insertion and withdrawal, as well as hydraulic-pressure-driven rapid scram insertion in response to reactor protection system signals. In the case of a scram, the hydraulic system is able to fully insert the control rods in 2.80 s. The electric motor also serves as the hydraulic scram's redundant control rod run-in.

The hydraulic pressure is supplied by pressurized water from the HCU accumulator via the scram inlet line. During normal operation, the control rod drive hydraulic subsystem provides high pressure water to charge the accumulator and purge water flow to the FMCRDs.

There are 205 FMCRDs in housings welded into the RPV bottom at ABWR. Each FMCRD has a hollow piston tube that can be moved by a ball nut and a ball

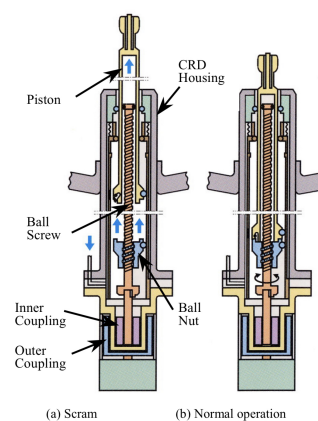


Figure 1.3: Operation modes of FMCRD

screw powered by an electric stepping motor. A bayonet coupling connects the upper end of the piston to the bottom of the control rod and cannot be decoupled without rotation.

There are 103 HCUs, each of which has enough water to quickly insert two FM-CRDs. A pre-pressurized accumulator supplies the pressurized water.

During a scram, the water is discharged into the RPV, eliminating the scram discharge line and simplifying the system.

The following are the advantages of FMCRD:

- Fine motion control by the electric motor (in previous versions of BWR, the rods could only be placed in a limited number of positions),
- Short startup time with automatic gang operation,
- Streamlined and simplified HCU system,
- Reduced occupational radiation exposure during its maintenance, and
- Highly reliable coupling between CRD and control rod with separation detection system.



The independent and precise control of the control rods allows to precisely regulate the reactivity inside the core, and the FMCRD is a great improvement brought by the ABWR. This fine control also facilitates the operation of the reactor in a load-following mode as smaller power changes

1.3.6 Reactor auxiliary system

The main auxiliary systems in the ABWR are the reactor building cooling water (RBCW) system, the reactor water cleanup (RWCU) system, the fuel pool cooling and cleanup (FPCU) system, and the suppression pool cleanup (SPCU) system. Furthermore, there are many other auxiliary systems such as instrument and service air, condensate and demineralized water transfer, chilled water, HVAC, equipment drain, floor drain, and other systems that are essentially the same as on previous BWR plants and are not covered here because the designs are all well proven.

The RBCW system consists of piping, valves, pumps, and heat exchangers that provide cooling water. To provide cooling water to the equipment the system is divided into three ECCS and RHR safety, each with its own pump and heat exchanger.

The RBCW system also provides cooling water to equipment in non-safety systems such as the RWCU, FPCU and other systems and equipment that require cooling water.

Depending on the unique site conditions, the RWCU heat exchangers are cooled by water from the plant service water or the ultimate heat sink.

The RWCU system is made up of piping, valves, pumps, heat exchangers, and filter demineralizers that are used to remove impurities from the reactor primary coolant water and keep it within acceptable limits during the plant's various operating modes. The RWCU design for the ABWR is essentially the same as that of previous BWRs, with the following exceptions:

1. The RWCU pumps are located downstream of the regenerative and non-regenerative heat exchangers to reduce pump operating temperature and improve pump seal and bearing performance, and
2. Two 1% capacity systems are used instead of only one 1% system, as in previous BWRs.

The FPCU and SPCU systems are made up of piping, valves, pumps, heat exchangers, and filter-demineralizers that are used to remove decay heat from the spent fuel storage pool as well as impurities from the water in the spent fuel pool, dryer/separator pool, and suppression pool in order to keep water quality within acceptable limits during different plant operating modes. The FPCU system's filter-demineralizer is shared by the SPCU system for cleaning the suppression pool water. The FPCU and SPCU systems are virtually identical to those found on previous BWRs.

1.4 Operating characteristics

The ABWR design includes extensive automation of operator actions required during normal plant startup, shutdown, and power range maneuvers. In comparison to conventional BWR designs, the automation features used in the ABWR are intended to improve operability and capacity factor. The level of automation implemented in the ABWR, on the other hand, has been carefully chosen to ensure that the primary control of plant operations remains with the operators. The operators are fully aware of the plant's status and can intervene at any time if necessary.



The ABWR control room design allows a single operator to perform all required control and monitoring functions both during normal plant operations and during emergency plant conditions. Rather than the traditional role of monitoring and controlling individual system equipment, the operator's primary responsibility will be to monitor the status of individual systems and the overall plant, as well as the progress of automation sequences. The operating staff organization for the reference ABWR control room design, on the other hand, is based on having two operators normally stationed at the control console to foster a team approach in plant operation and to maintain operator vigilance.

With the addition of reactor internal pumps (RIPs), power changes of up to 30% of rated power can be accomplished automatically through recirculation flow control alone, providing the ABWR with automatic electrical load-following capability without the need to adjust control rod settings. During normal operation, the ABWR fine-motion control rod drives (FMCRDs) are moved electronically in small increments, allowing for precise power management. During an emergency shutdown, the FMCRDs are hydraulically inserted into the core, with a backup provision for continuous electronic insertion.

Design	Reactor type	Maximum load change rate	Load cycling range
ABWR [285]	BWR	60%/min	65%–100%
AP1000 [286]	PWR	5%/min	15%–100%
EPR [287]	PWR	5%/min	60%–100%
		2.5%/min	25%–60%
ESBWR [288]	BWR	N/A	50%–100%
Konvoi [283, 289]	PWR	2%/min	20%–100%
		5.2%/min	50%–100%
		10%/min	80%–100%
SWR 69 [283]	BWR	3.8%/min	60%–100%
		10%/min	90%–100%
SWR 72 [283]	BWR	4.6%/min	60%–100%
		10%/min	90%–100%
Vor-Konvoi [283]	PWR	4.4%/min	50%–100%
		10%/min	80%–100%
VVER-1000/1200 (V-392 and V-491) [287]	PWR	5%/min	50%–100%
		10%/min	±20%

Figure 1.4: Load change rates for different reactors

Under normal operation conditions, load-following can be achieved using the RIP only when we consider a power change of less than 30% of rated power. However, when a change of more than 30% of rated power is needed, the FMCRD systems also allow load-following. In figure 1.4, we can see that the maximum load change rate is extremely high compared to other reactors : 60%/min. This is one of the great strengths of ABWR. However, we need to nuance a bit that number : this applies only when load-following is achieved only using the RIP. When a change of more than 30% of rated power is needed, the control rods are moved and the maximum load change rate becomes 2.5% per minute, which is still significantly faster than needed to respond to load and frequency changes.



Now that we have seen the main operating principles during normal operation, we will now talk about key procedures : startup and shutdown of the reactor. As it has already been said, startup of the reactor is entirely automated. Reactor controls are fully digital (with redundant digital and manual backup) but the goal is not to replace the operators but to simplify their work. The operators still initiate the automated sequences included in the startup procedure and check that all the prerequisites are satisfied : the ECCS and other critical safety systems need to be tested before proceeding to the startup of the reactor. Moreover, the computer can ask operators to take action at any time.

The path followed during startup is represented by the arrows on the power-flow map of the ABWR :

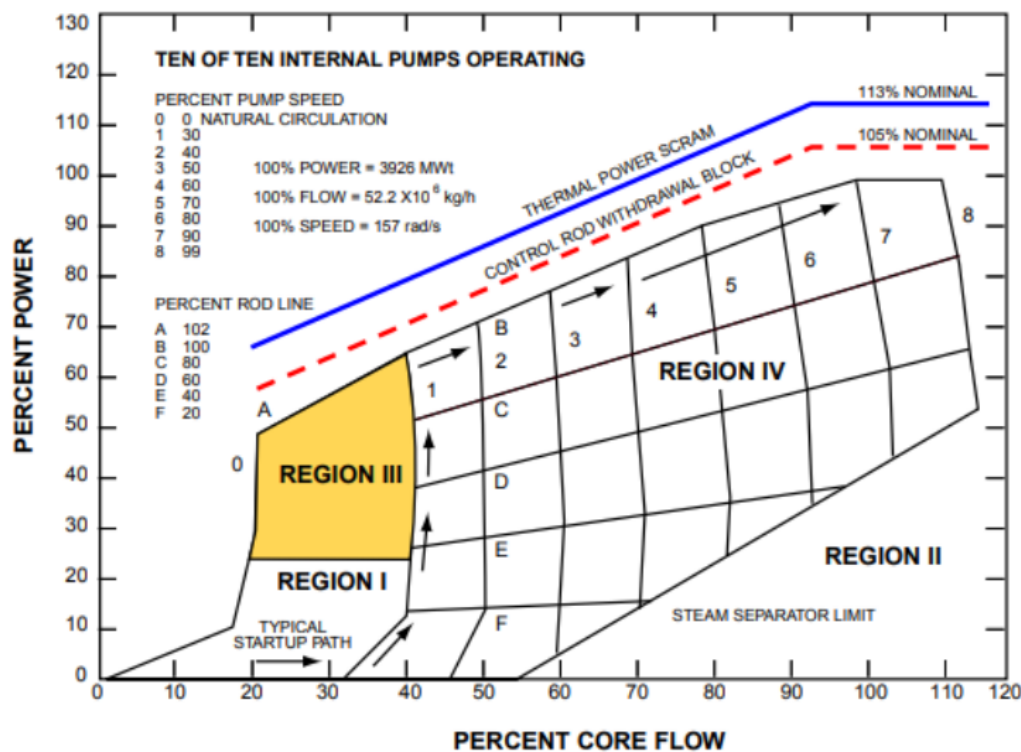


Figure 1.5: ABWR power-flow map

In the beginning of startup, when all the prerequisites are satisfied, the core flow is progressively increased until reaching about 30% of the rated core flow. Then, the control rods, which were previously fully inserted, are slowly withdrawn from the core until criticality is reached. Then, at about 32% power, the core flow is increased again and further withdrawal of the control rods allows the power to increase. Control rods are withdrawn until reaching about 70% of rated power. From there, the output power is only modified using the RIPs. This procedure allows the reactor to reach 100% power from cold shutdown conditions in about 25 hours, and to reach 100% power from hot shutdown conditions in only about 5 hours.

During shutdown of the reactor, the reverse process occurs. Core flow is decreased and control rods are inserted in the core in order not to reach the instability region.

Normally, during shutdown, the RIP keep running at minimum speed until the reactor vessel is entirely flooded in preparation for refueling. If water level goes above the separator spillover, natural circulation alone is sufficient to transfer the core decay heat to the downcomer region where it is removed by the RHR (Residual Heat Removal system).

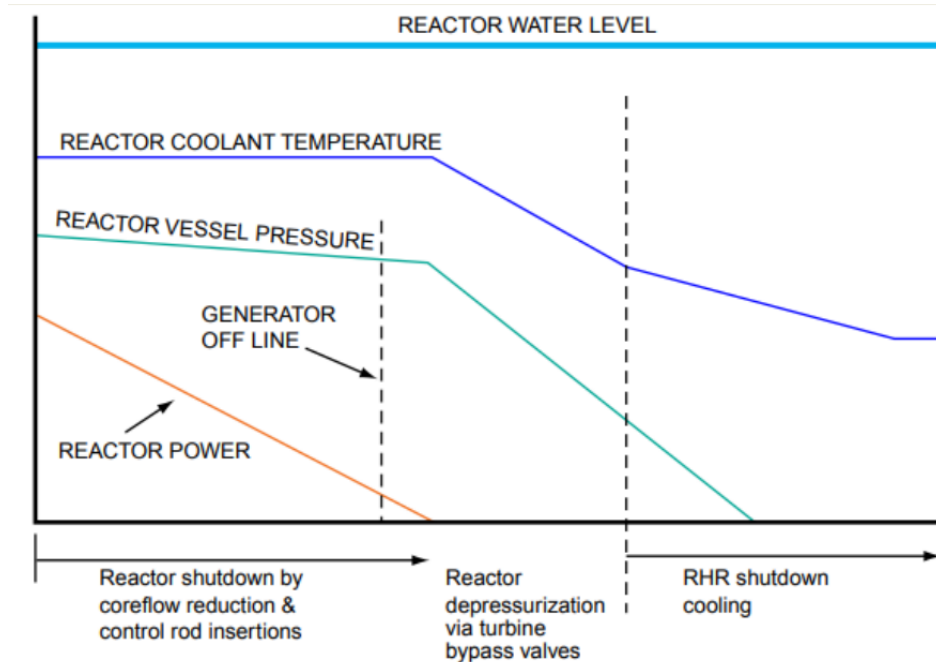


Figure 1.6: ABWR shutdown sequence

1.5 Safety

1.5.1 Active, passive and inherent safety

- The ABWR ECCS network underwent changes to become a three-division system with both high and low-pressure injection pumps and heat removal capabilities in each division.
- To increase diversity, one of the systems, the RCIC system, now includes a steam-driven high-pressure pump. Transient response was improved by adding three high-pressure injection systems in addition to feedwater.
- To reduce the risk of a "station blackout," three on-site emergency diesel generators were installed to support core cooling and heat removal, along with an on-site gas turbine-generator.
- The balanced ECCS system relies less on the automatic depressurization system (ADS) function since a single motor-driven high-pressure core flooder (HPFL) is designed to maintain core coverage for any potential line break size.
- The adoption of fine motion control rod drives (FMCRD), which allow reactor shutdown via hydraulic or electric insertion, improved response to anticipated transients without scram (ATWS).

- Furthermore, automation of emergency procedures such as feedwater runback and standby liquid control (SLCS) injection eliminated the need for immediate operator action to mitigate an ATWS.

1.5.2 Severe accidents

The US ABWR also improved its ability to mitigate severe accidents, despite the fact that such occurrences are extremely unlikely, by:

- Containment integrity threats from hydrogen generation were eliminated through inerting.
- Cooling of postulated core debris is ensured by sufficient spreading area in the lower drywell and a passive drywell flooding system.
- Manual connections allow for the use of on-site or off-site fire water systems to keep the core cool.
- Finally, a passive hard-piped wetwell vent controlled by rupture disks set at twice design pressure (service level C) is designed to prevent catastrophic containment failure and provide maximum fission product "scrubbing" to reduce off-site consequences.

1.6 Summary

The ABWR was created by combining the most advanced technologies and operational experiences. It improves the BWR design in a variety of ways. The use of reactor internal pumps (PIRs) and fine motion control rod drives (FMCRDs) in the primary system has significantly improved the design.

The "test before use" principle guided the development of the ABWR primary system component. Extensive testing was carried out to confirm the performance and reliability.

2. Calculation of selected core parameters

In this section we will study the pressure and temperature characteristics in the axial direction in an average fuel channel. The key parameters required to conduct calculations for this reactor are listed in Table 1. The following core-averaged thermal-hydraulic characteristics are calculated using these parameters and presented as plots:

- Axial pressure drop distribution
- Axial coolant enthalpy distribution
- Axial coolant temperature distribution
- Axial void fraction distribution
- Flow characteristic of the core

Parameters	
Total core heat output	3926 MWth (*1.05)
Nominal system pressure	7.07 MPa
Total core mass flow rate	52.5 Mkg/h
Inlet temperature	278 °C
Mass flow rate	15333 kg/s
Number of fuel assemblies	872
Number of fuel rods	92
Number of spacers	8
Fuel assembly pitch	15.5 cm
Active fuel height	447 cm
Clad Thickness	0.066 cm
Outside fuel rod diameter	1.026 cm
Diameter of fuel pellets (UO_2)	0.876 cm
Clad and channel wall roughness	1.5 μ m

Table 1: Parameters used for the calculations

2.1 Power Distribution

The typical power distribution for a cylindrical core is given by,

$$q''(r, z) = q_0'' J_0 \left(\frac{2.405r}{\tilde{R}} \right) \cos \left(\frac{\pi z}{\tilde{H}} \right) \quad (2.1)$$

where, q_0'' is the power per rod, J_0 is the Bessel function and \tilde{H} is the extrapolated height and is given by $H/\tilde{H} = 5/6$. For this section we assume the power distribution in the radial direction to be constant. So the power in the axial direction is just given by:

$$q''(z) = q_0'' \cos \left(\frac{\pi z}{\tilde{H}} \right) \quad (2.2)$$



To calculate the power distribution of an average channel in the axial direction we divide the fuel rod into cells of uniform height (we used 80 cells), and obtain the power distribution for each cell $q_{cellAve}$ using the following formula,



$$q_{cell}(z) = q_{cellAve} * f_z * \cos\left(\frac{\pi z}{H_e}\right) \quad (2.3)$$

where f_z is the axial peaking factor given by

$$f_z = \frac{\pi H}{2\tilde{H} \sin\left(\frac{2.405H}{\tilde{H}}\right)}$$

The power distribution observed for ABWR with power specification unique to our project (given in Table 1), in the axial direction, with the scale on the x-axis going from $(-H/2, 0, H/2)$ is shown in Figure (2.1). The power distribution is a cosine function, with maximum power in the middle of the core.

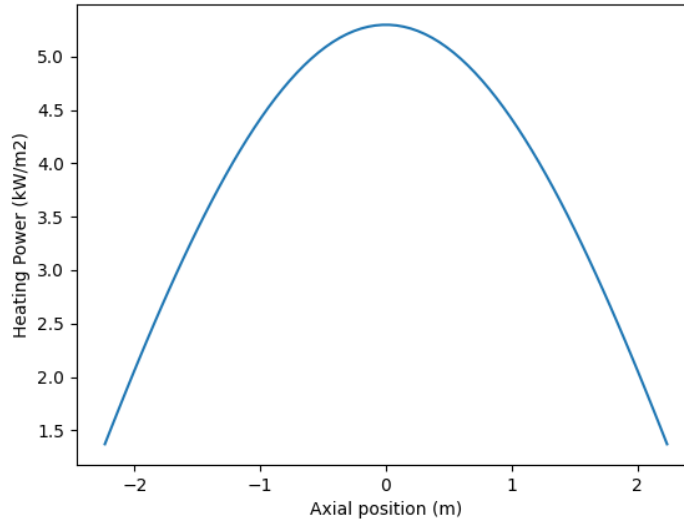


Figure 2.1: Power distribution in the axial direction

2.2 Enthalpy distribution

The enthalpy at the inlet of the system ($i(0)$) can be found from the XSteam function of python, as a function of the operating pressure and the inlet temperature. With that the rest of the enthalpies can be calculated using the energy balance equation as shown in the code below.

```
1 # cell enthalpies
2 i = np.zeros(len(z))
3
4 i[0] = steam_table.h_pt(P_operating, T_inlet)
5 for j in range(1, N_cell):
6     i[j] = i[j - 1] + q_cell_z[j - 1] / W * N_fr #Energy balance Eq.
```

Code extraction 1: Enthalpy distribution

With the enthalpy of the system, the equilibrium quality can be calculated for every cell using the formula:

$$x_e(j) = \frac{i(j) - i_l}{i_g - i_l}$$

where i_g and i_l are functions of the operating pressure (7.07 MPa), calculated using the XSteam package in Python.

Figure 2.2 (just below) shows the plot of the enthalpy along the axial direction. The maximum enthalpy obtained at the top of the reactor is almost 1550 kJ/kg. The shape of the curve corresponds to what was expected given the heating power distribution : the fastest increase in enthalpy takes place in the middle of the core, where the heating power is the highest.

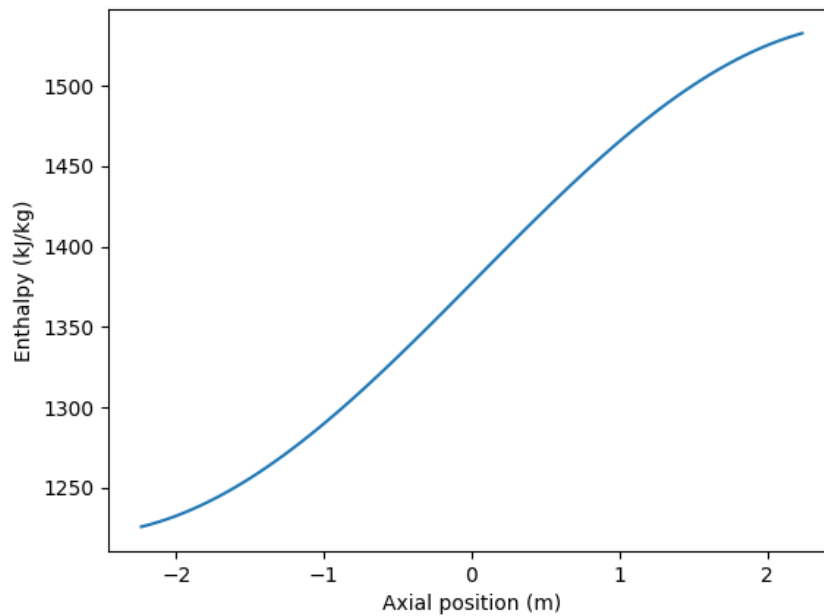


Figure 2.2: Axial distribution of enthalpy

Figure 2.3 (just below) shows the equilibrium quality along the axial direction. We can observe that at the inlet, we have single phase flow, where $x_e < 0$ and then we have two-phase flow, which is characteristic to boiling water reactors. We can see on this graph that boiling starts about 1m above the bottom of the core. The shape of the quality is identical to the shape of the enthalpy, which was expected as quality is an affine function of enthalpy.

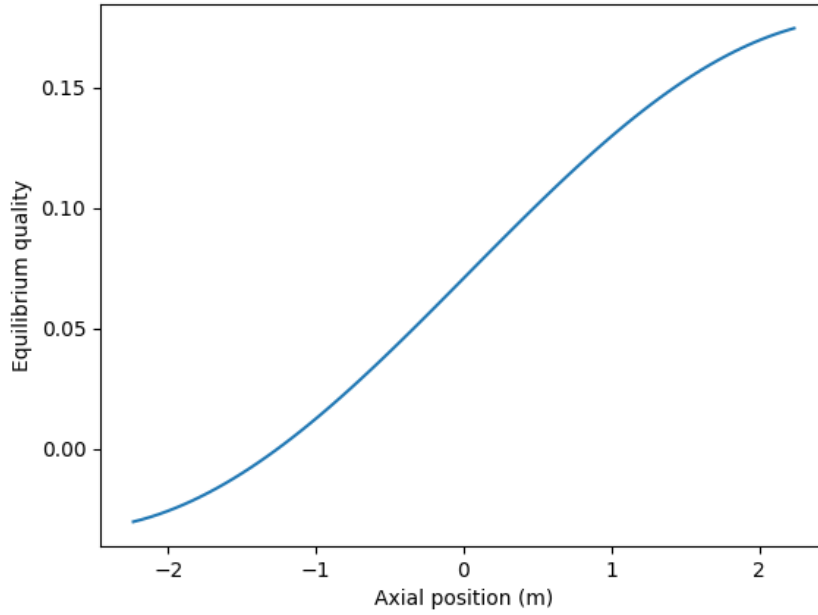


Figure 2.3: Equilibrium quality as a function of height

2.3 Pressure Drop

The pressure drop was one of the most complex parameters to calculate as it is influenced by a multitude of different factors. It is hard to take into account all of those influences, but we tried to be as accurate as possible and we took into account the impact of gravity, friction, acceleration, but also local pressure drops caused by spacers in the core, by the interruption of part-length rods or by the inlet and outlet. We also took into account the fact that in the bottom of the core, the coolant is a single phase flow and above the boiling point it becomes a two phase flow.

This is why, in the calculation of the pressure drop in the system, we start with calculation the void fraction. The void fraction helps us understand where the boiling starts in the reactor. The value of the void fraction is $\alpha = 0$ when $x_e < 0$, and for $0 < x_e < 1$, α is calculated as follows :

$$\alpha(z) = \frac{1}{1 + \frac{\rho_g}{\rho_f} \left(\frac{1-x_e(z)}{x_e(z)} \right)} \quad (2.4)$$

The void fraction along the axial direction for an average channel is shown in Figure (2.4). We see that initially the void fraction is constant at 0 and then it starts to rise, indicating the start of boiling in the reactor. The maximum void fraction achieved in this reactor is 0.8. Void fraction for normal operation cannot be equal to 1, which indicates an unsafe reactor.

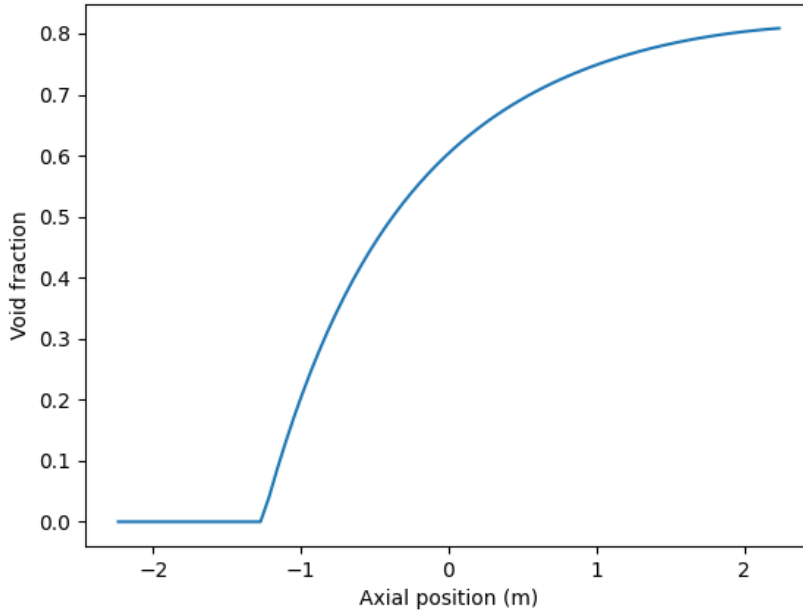


Figure 2.4: Axial void fraction distribution

The total pressure drop consists of the fuel channel pressure drop and the inlet and outlet orifices pressure drop:

$$(-\Delta p)_{\text{Total}} = (-\Delta p)_{\text{FuelChannel}} + (-\Delta p)_{\text{Orifice}} \quad (2.5)$$

The inlet orifices pressure loss accounts for about 50% of the total pressure drop in the core at nominal operating conditions and can be calculated by:

$$|(-\Delta p)_{\text{Orifice}}| = \xi_{\text{orifice}} \frac{G^2}{2\rho_{\text{in}}} \quad (2.6)$$

Since ξ_{orifice} is unknown, we can set the initial value for inlet orifices pressure loss and iterate to get the convergent value.

The pressure drop in the fuel channel mainly consists of the local pressure drops, the friction pressure drop, the gravity pressure drop and the acceleration pressure drop.

$$-\Delta p = \underbrace{r_3 C_{f,lo} \frac{4L}{D} \frac{G^2}{2\rho_f}}_{\text{friction}} + \underbrace{r_4 L \rho_f g \sin \varphi}_{\text{gravity}} + \underbrace{r_2 \frac{G^2}{\rho_f}}_{\text{acceleration}} + \underbrace{\left(\sum_{i=1}^N \phi_{lo,d,i}^2 \xi_i \right) \frac{G^2}{2\rho_f}}_{\text{local}} \quad (2.7)$$

where $C_{f,lo}$ is given by Haaland correlation* and $Re = \frac{G d_h}{\mu}$. r_2, r_3 and r_4 are the multipliers which are equal to 1 in single phase flow and are calculated using the following expressions for two phase flow.

- Friction multiplier:

$$r_3 = \frac{1}{L} \int_0^L \phi_{lo}^2 dz$$



- Gravity multiplier:

$$r_4 = \frac{1}{L\rho_f} \int_0^l [\alpha\rho_g + (1-\alpha)\rho_f] dz$$

- Acceleration multiplier:

$$r_2 = \left[\frac{x^2\rho_f}{\alpha\rho_g} + \frac{(1-x)^2}{(1-\alpha)} \right]_{ex} - \left[\frac{x^2\rho_f}{\alpha\rho_g} + \frac{(1-x)^2}{(1-\alpha)} \right]_{in}$$

- The local pressure drop is mainly due to the spacers. The formula is given as a sum of $\phi_{lo,d,i}^2$ and ξ is given by,

$$\phi_{lo,d,i}^2 = 1 + \left(\frac{\rho_f}{\rho_g} - 1 \right)$$

$$\xi_i = a_1 + a_2 \cdot \text{Re}^{-b}$$

where the a_1 , a_2 and b are constants found in literature.

Other important formulas used for the calculation of the pressure drop in the reactor are:

- Haaland correlation: $\frac{1}{\sqrt{C_f}} = -3.6 \log_{10} \left[\left(\frac{k/D_h}{3.7} \right)^{1.11} + \frac{6.9}{\text{Re}} \right]$
- Hydraulic diameter: $D_h \equiv \frac{4A}{P_w} = \frac{4w^2 - N\pi d_r^2}{4w + N\pi d_r}$
- Wetted perimeter: $P_w = 4w + N\pi d_r$
- Heated diameter: $D_H \equiv \frac{4A}{P_H} = \frac{4w^2 - N\pi d_r^2}{N_{FR}\pi d_r}$
- Heated perimeter: $P_H = N_{FR}\pi d_r$

Finally, after running those calculations, we are able to calculate the pressure (and of course the pressure drop) for every height in the average channel.

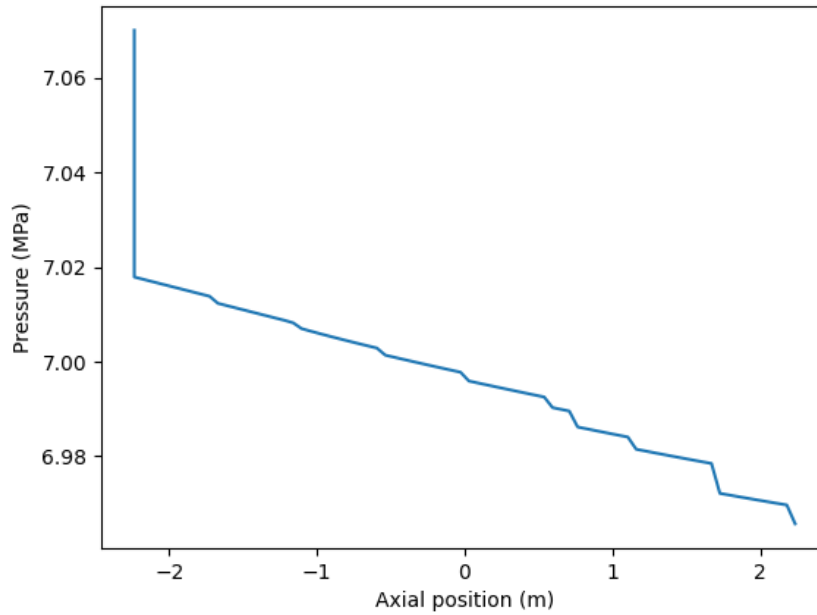


Figure 2.5: Axial pressure distribution

Figure (2.5) shows the axial pressure distribution obtained for ABWR with characteristics from Table (1). As expected in BWRs we observe that the inlet orifice pressure drop is 50% of the total pressure drop.

Several breaks are visible in the curve. Most of them are caused by the spacers, which are responsible of 7 drops in this graph. We can see only 7 pressure drops caused by the spacers even if there are 8 spacers in the core because we found in literature that the eighth spacer is located a little bit above the core active height. We can notice that the pressure drops caused by the spacers increase when the void fraction increases. The breaks caused by the spacers are quite regularly spaced but we can notice a steep drop at two thirds of the total height. This steep drop is caused by the ending of 14 part-length rods. When those part-length rods end, the area available for the coolant to flow brutally increases, causing turbulence in the flow and thus a pressure drop. The last drop in the graph corresponds to the outlet pressure drop.

2.4 Coolant temperature distribution

The coolant temperature can be simply found in python using XSteam as a function of the changing pressure and enthalpy.

```
1 #Coolant temperature distribution
2 Temperature = np.zeros(N_cell)
3 for k in range(N_cell):
4     Temperature[k] = steam_table.t_ph(p[k], i[k])
5     Temperature[k] -= 273.15 #conversion from kelvin
6
7 plt.plot(z, Temperature)
8 plt.ylabel('Temperature (C)')
9 plt.xlabel('Axial position (m)')
```

```
plt.show()
```

Code extraction 2: Coolant temperature distribution

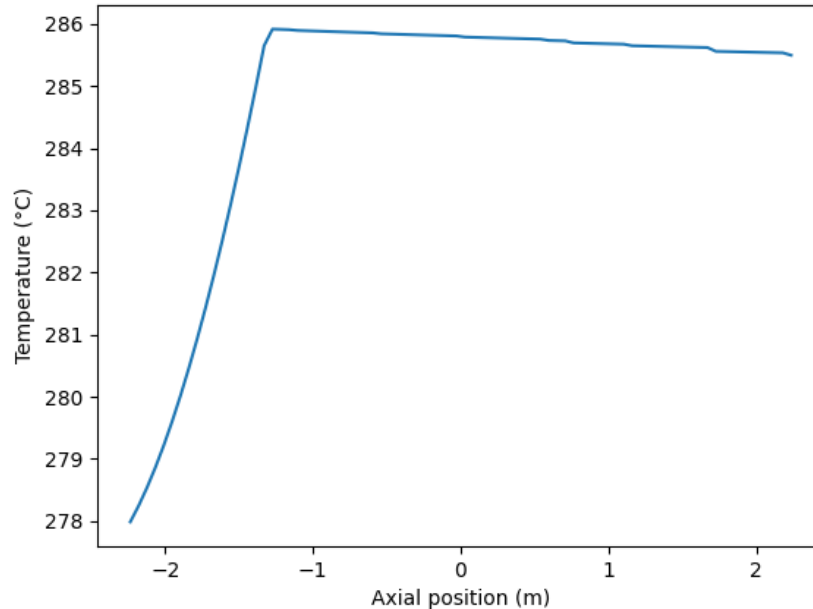


Figure 2.6: Axial temperature distribution

The temperature in the reactor rises to reach a saturation temperature at 7.07 MPa, at 286.5°C, as seen in the Figure (2.6). At saturation temperature, when boiling is achieved, the curve becomes almost constant because all the energy is used up in phase change so no more rise is observed. Actually, the temperature even decreases a bit because of the pressure drop : as pressure decreases when the coolant rises through the core, the saturation temperature also decreases.



2.5 Flow characteristics of the core

In this section the relationship of change in pressure as a function of mass flow rate, $\Delta p = f(G_{core})$, is studied. To achieve this, the core power is kept at 0%, 50%, 100% and 150% of the nominal power, with the mass flow rate varying from 1% to 150% of the core nominal flow.

```
1 Powers = [0, 50, 100, 150]
2 Affichage_pressure_drop = np.zeros((len(Powers),150))
3
4 for m in range (len(Powers)):
5     for n in range (1,151):
6
7         Q_tot = 3926 * 1.05e6 * Powers[m]/100
8         W = 15333 * n/100
```

Code extraction 3: Core flow characteristics

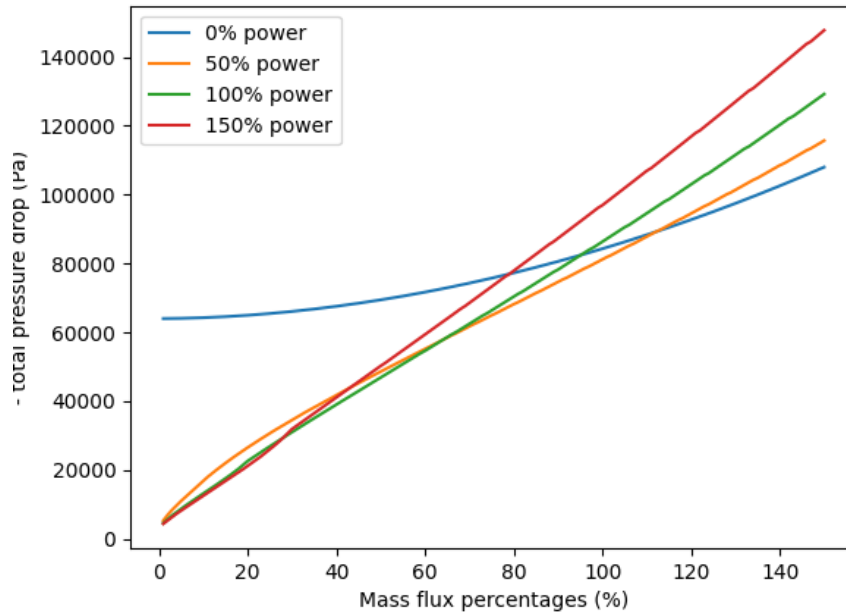


Figure 2.7: Core flow characteristics

Figure 2.7 is the graph that we obtained after running our code. The first striking thing is that no matter what is the output power, the pressure drop increases with core flow. That was expected since the expressions of the majority of the contributions to pressure drop increase when G increases (not the gravity pressure drop though). For example, the friction pressure drop becomes higher when the core flow is higher because coolant loses more energy when it runs at higher speeds.

What is also striking is that the 0% curve is far above the others when core flow is low. This is caused by the gravity pressure drop : the more liquid is present in the channel the higher the pressure drop is. When the core flow is only a few percents of rated core flow, the coolant moves slowly and spends a lot of time in the core being heated. Thus, when the core flow is low, coolant evaporates quickly and almost only steam can be found in the core, even if the heating power is low, so in that case the gravity pressure drop is very low (this is dangerous and doesn't happen in normal operation). However, when power is 0% of rated power, even if the core flow is low, only water can be found in the core, so the gravity pressure drop is much higher. This is also because of gravity pressure drop that the pressure drop is higher with 50% power than with 100% or 150% power when the core flow is low. Then, the other contributions counterbalance this effect.

3. Calculation of CHF margins in a hot channel

In the previous section, we studied the distribution in an average channel. In this section we will study the distribution in a hot channel and find the condition where dryout type CHF is achieved. The following results are presented as plots for a hot channel:

- Axial pressure drop distribution
- Axial coolant enthalpy distribution
- Axial coolant temperature distribution
- Axial void fraction distribution
- Minimum critical power ratio (MCPR)

3.1 Power distribution

As explained in the previous section, the power distribution is given by Equation (2.1). To calculate the power distribution in a hot channel, an additional radial peaking factor, given by Eq.3.1, is added to Equation (2.3) to obtain Equation (3.2).

$$f_R = \frac{2.405R}{2\tilde{R} \cdot J_0\left(\frac{2.405H}{H_e}\right)} \quad (3.1)$$

$$q_{\text{cell}}(z) = q_{\text{cellAve}} * f_R * f_z * \cos\left(\frac{\pi z}{H_e}\right) \quad (3.2)$$

The power distribution observed for a hot channel is similar to the one observed in an average channel, only difference is that the power is higher in case of the hot channel. Figure 3.1 shows the power distribution in a hot channel.

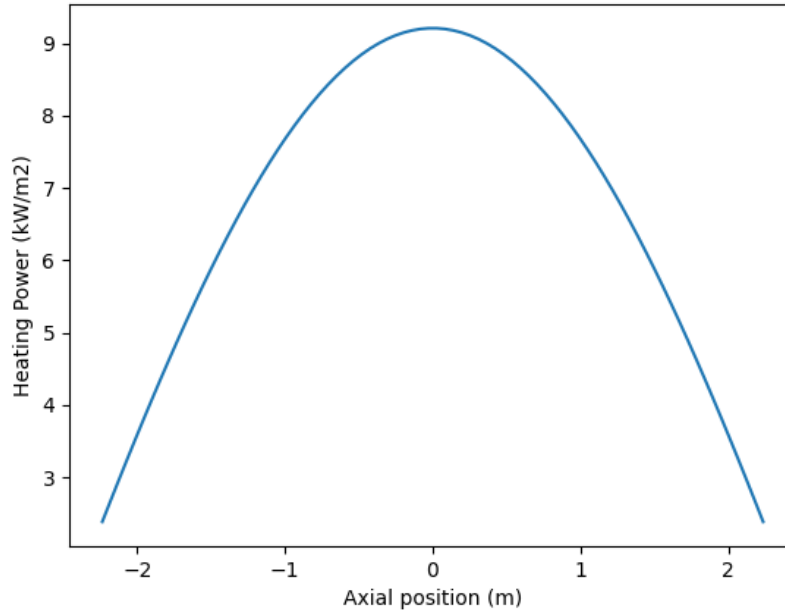


Figure 3.1: Power distribution in a hot channel

3.2 Enthalpy

As explained in Section 2.2, the enthalpy depends on the power. When the power rises (as seen in Figure 3.1) the corresponding enthalpy also rises (as seen in Figure 3.2).

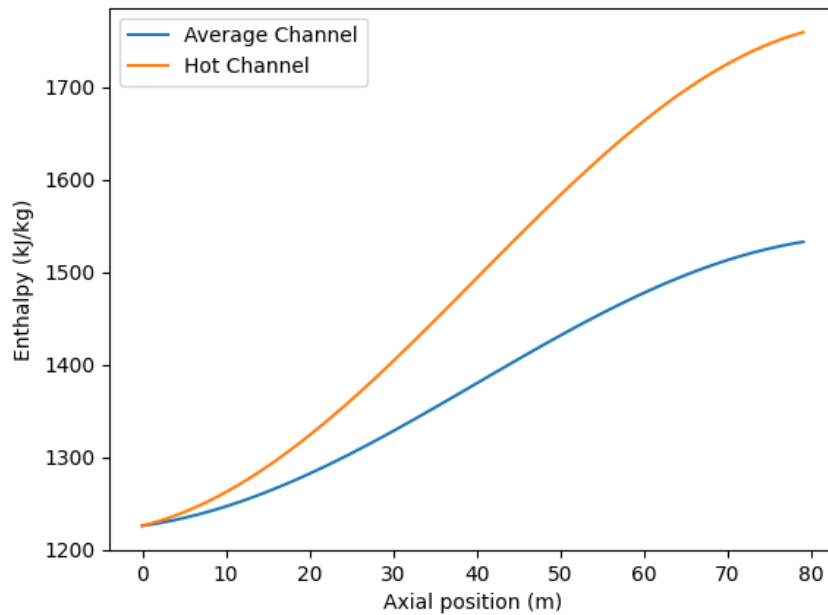


Figure 3.2: Comparison of enthalpy in a hot channel and an average channel

The quality in the hot channel can be calculated using the following formula:

```

1 # equilibrium quality calculus
2
3 x_eq = np.zeros(N_cell)
4
5 i_satl_1st = steam_table.hL_p(P_operating)
6 i_satg_1st = steam_table.hV_p(P_operating)
7 x_eq[0] = (i[0] - i_satl_1st)/(i_satg_1st - i_satl_1st)

```

Code extraction 4: equilibrium Quality

In Figure 3.3, it is observed that the output quality doubles when we move from an average channel to a hot channel (it goes from 0.16 in average channel to about 0.32 in hot channel). It is to be noted that it is still within the theoretically expected values.



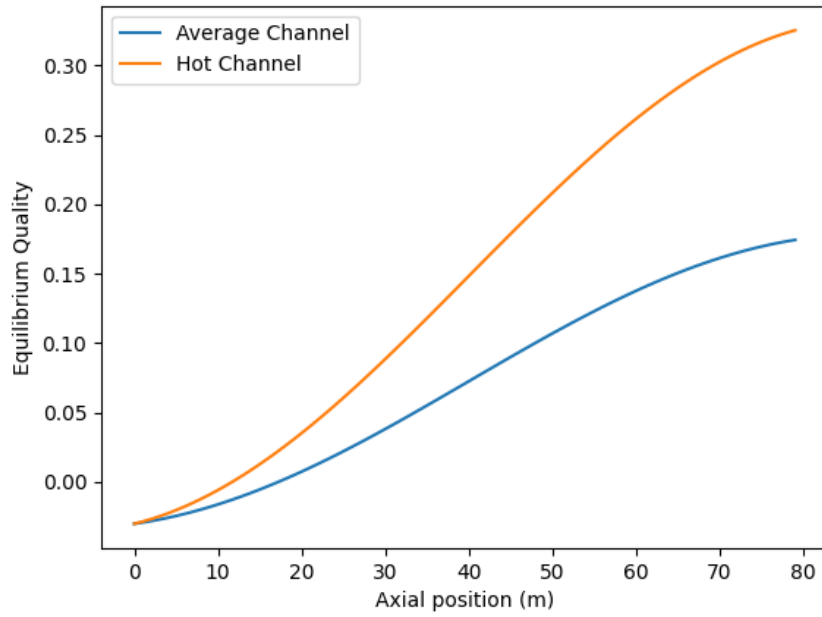


Figure 3.3: Comparison of quality in a hot channel and an average channel

3.3 Pressure Drop

In a hot channel we expect the boiling to start sooner as the quality goes sooner above 0. This can be observed in the plot showing the void fraction along the axial direction, in Figure 3.4. It is also interesting to notice that the void fraction reaches about 0.9 in hot channel.

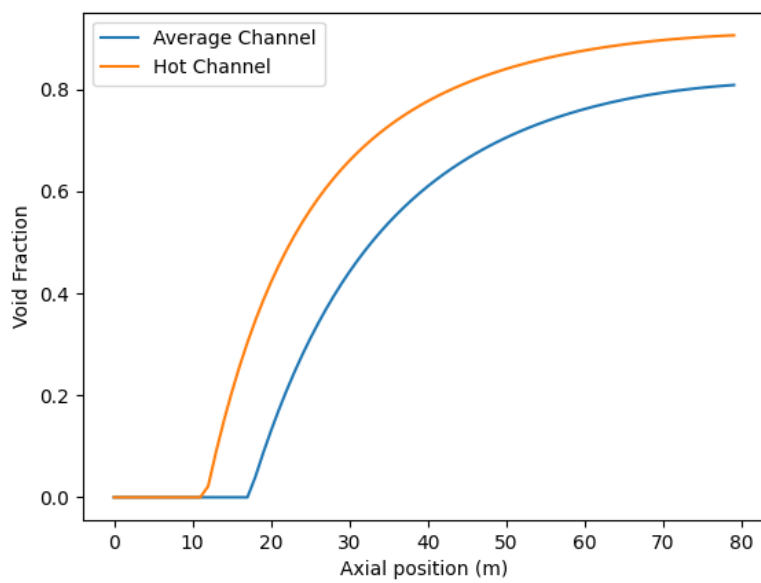


Figure 3.4: Comparison of void fraction in a hot channel and an average channel

As discussed before in section 2.5, the pressure drop increases with power. This is because some contributions to the pressure drop are higher when the output power is higher : for example the friction pressure drop and the acceleration pressure drop. In our case, we can refer to figure 2.7, and we can see that with 100% core flow, when power is increased, the pressure drop increases too, so what we obtain here was totally expected.

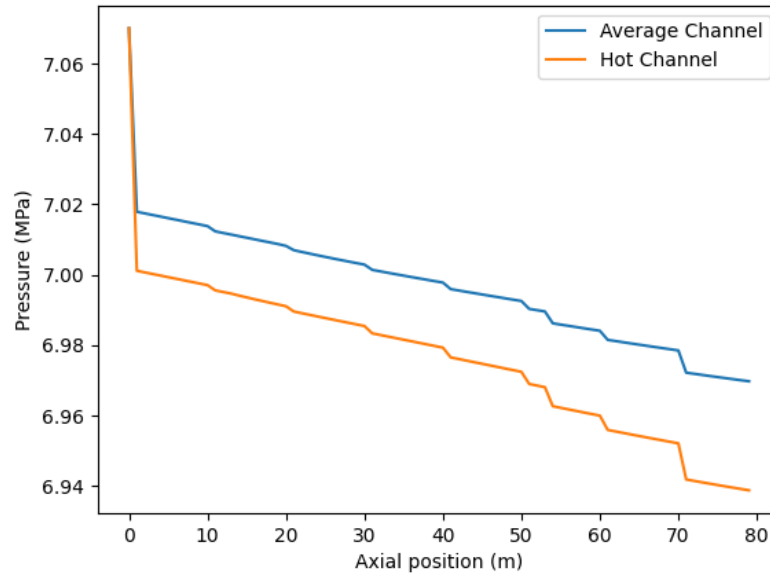


Figure 3.5: Comparison of pressure drop in a hot channel and an average channel

3.4 Coolant temperature distribution

The coolant temperature is a function of pressure drop and enthalpy. In a hot channel, enthalpy increases a lot while pressure approximately the same as in an average channel, so the coolant temperature also increases. The boiling in a hot channel starts earlier than in an average channel, therefore we observe a steeper rise in coolant temperature in the beginning, as seen in Figure (3.6). The temperature again reaches the saturation temperature at 286.5°C corresponding to 7.07MPa . However, after reaching 286.5°C , the temperature slowly decreases as in an average channel, but it is a bit lower than the temperature in an average channel. That is because the pressure drop is higher in hot channel, so pressure is lower and saturation temperature is lower too.

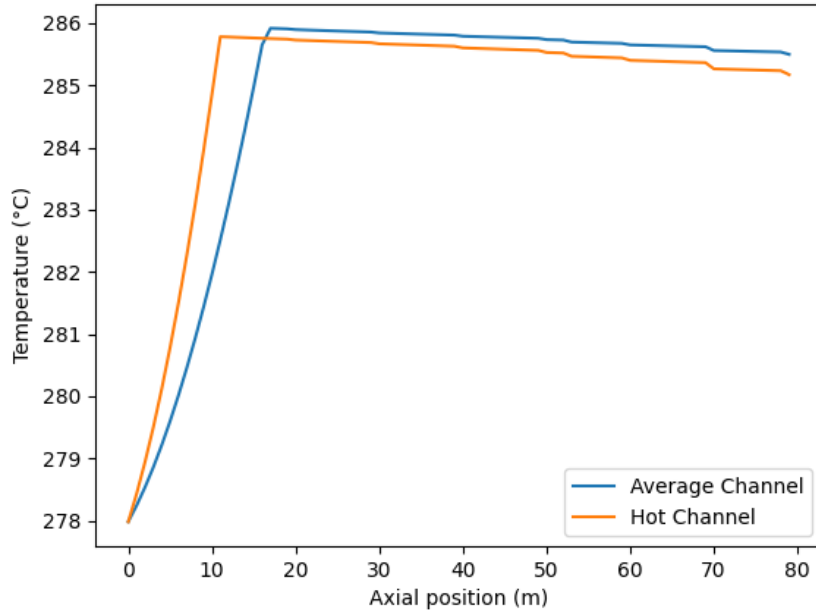


Figure 3.6: Comparison of coolant temperature in a hot channel and an average channel

3.5 Dryout type CHF calculation



The **dryout-type CHF** typically occurs in the annular flow regime where a liquid film covers the heated rod surface and saturated vapor flows in the core region. This is dangerous to have in a reactor, therefore this section makes calculations to understand the threshold where dryout occurs in the reactor, so that it can be avoided. There are various correlations that can be used to calculate the dryout in ABWR. To have a good grasp of the actual answer, we apply at least two correlations to have a better understanding.

3.5.1 Levitan-Lantsman correlation

Levitan-Lantsman correlation is a simple correlation which depends only on the operating pressure, p (in bars) and mass flow rate, G . The critical quality for a rod of 8mm is given by,

$$x_{cr|_{8mm}} = \left[0.39 + 1.57 \frac{p}{98} - 2.04 \left(\frac{p}{98} \right)^2 + 0.68 \left(\frac{p}{98} \right)^3 \right] \left(\frac{G}{1000} \right)^{-0.5}$$

.

To find the critical quality for a rod larger than that we can use the equation,

$$x_{cr} = x_{cr|_{8mm}} \cdot \left(\frac{8}{D_h} \right)^{0.15}$$

where D_h is the hydraulic diameter. The critical quality found by this method for ABWR with the unique specifications from Table 1 is $x_{cr} = 0.61067$.

The minimum critical power ratio is given by :

$$MCPR = \frac{\text{critical power in hot channel, } q_{cr}}{\text{actual power in hot channel, } q_{ac}} \quad (3.3)$$

Our goal is thus to determine q_{cr} and to do so, we used this code :

```
1 # checking for critical power
2 n=0
3 while x_eq[N_cell-1] < x_cr:
4     Q_tot = 3926 * 1.05e6 * (1 + n/1000)
```

Code extraction 5: Critical power

In this code, we start from the actual power in the hot channel, and we slowly increase it until the output quality, which is the highest quality in the core, is equal to the critical quality.

The minimum critical power ratio (MCPR) found by this method is:

$$MCPR = \frac{q_{cr}}{q_{ac}} = 1.804$$

Figure 3.7 shows the quality in the core when $q = 1.804 * q_{ac}$. We can see that the output quality is actually equal to the critical quality that we have previously found.

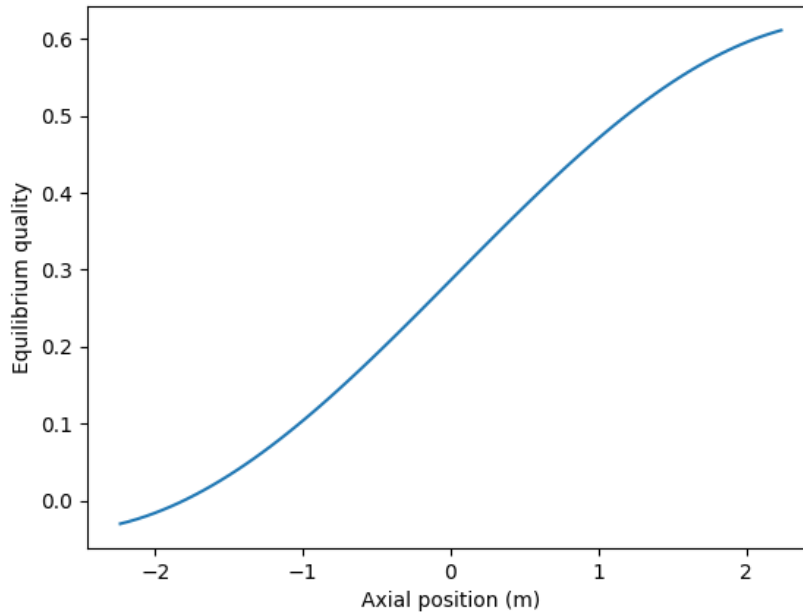


Figure 3.7: Critical quality distribution

The critical quality that we have found using this correlation is much higher than the output quality that we obtain with the actual distribution of power in a hot channel. Moreover, the MCPR is equal to 1.804, which is a lot over 1, so dryout seems to be very

unlikely to occur according to the results we obtained using this correlation. However, this correlation is quite simple and might not be extremely accurate for ABWr, so we also calculated the MCPR using another correlation to check our results : the Reddy and Fighetti correlation.

3.5.2 Reddy and Fighetti correlation

The Reddy and Fighetti correlation depends on mass flow rate, G , operating pressure, p , hydraulic diameter D_h , heated diameter, D_H , quality, x , inlet quality, x_{in} and the boiling length, L . The conditions to satisfy before using the formula include:

$$\begin{aligned} 147 < G < 3023 \text{ kg/m}^2 \text{ s} \quad & 13.8 < p < 169.9 \text{ bar} \quad & 8.9 < D_h < 13.9 \text{ mm} \\ 6.3 < D_H < 13.9 \text{ mm} \quad & -0.25 < x < 0.75 \quad & -1.10 < x_{in} \leq 0.0 \\ 0.762 < L < 4.267 \text{ m} \end{aligned}$$



The equation to calculate the critical power is thus given by,

$$q''_{cr}(\mathbf{r}) = B \frac{A - x_{in}}{C + \frac{x(\mathbf{r}) - x_{in}}{q''_R(\mathbf{r})}} \quad (3.4)$$

where

$$\begin{aligned} A &= a_1 p_R^{a_2} G_R^{(a_3 + a_4 p_R)} & G_R &= G/1356.23 \\ B &= 3.1544 \times 10^6 & p_R &= p/p_{cr} \\ C &= c_1 p_R^{c_2} G_R^{(c_3 + c_4 p_R)} & q''_R(\mathbf{r}) &= q''(\mathbf{r})/3.1544e6 \end{aligned}$$

With this correlation, we obtain the CPR in function of the position in the core, and the MCPR is found at the output of the core. The minimum critical power ratio that we found using this correlation is:

$$MCPR = \frac{q_{cr}}{q_{ac}} = 1.342$$

Even if the value is lower than the one found using the previous correlation, it is still significantly higher than 1, so dryout seems to be very unlikely to happen.

3.5.3 Conclusion

Using the two correlation we find that the minimum critical power ratio (MCPR) of our reactor is within the safe operational limits. The reason for them to be different from each other could be because in the case of Levitan-Lantsman correlation, the calculations are very simple and they only depend on two factors. While in case of Reddy and Fighetti correlation, the calculations are a bit more complex and depend on various parameters. Therefore the later correlation takes into account the changing parameters in the reactor more accurately and can be used as a reference.



4. Calculation of the maximum cladding and fuel pellet temperature

The fuel temperature in a reactor must never exceed the melting temperature of the fuel material. The clad temperature should also be checked to ensure that it does not exceed the maximum permissible value for the clad material. In this section we identify the locations where fuel maximum and clad maximum temperatures are reached and we calculate their values. Some additional parameters to keep in mind for this exercise are listed below in Table 2.

Parameters	
Total core heat output	3926 MWth (*1.05)
Nominal system pressure	7.07 MPa
Melting temperature of Zr-2 (clad)	1852 °C
Maximum allowed temperature of clad	1204 °C
Melting temperature of UO_2	2800°C
Maximum allowed temp. of fuel pellets	2200°C
Fuel assembly pitch	155 cm
Active fuel height	447 cm
Clad Thickness	0.66 cm
Outside fuel rod diameter	1.026 cm
Diameter of fuel pellets (UO_2)	8.76 cm
Clad and channel wall roughness	1.5 μ m

Table 2: Parameters used for the calculations

For calculations in this section, we again consider a hot channel, so that we can find the absolute maximum temperatures achieved by the fuel and clad. We began by calculating the temperatures at every interface : coolant/cladding, cladding/gas and gas/fuel. Then, we divided the fuel rod radially into cells and used the equations involving temperature in each layer (fuel, gas, cladding) to calculate accurately the temperature at every position in the fuel rod (every height and every radius).

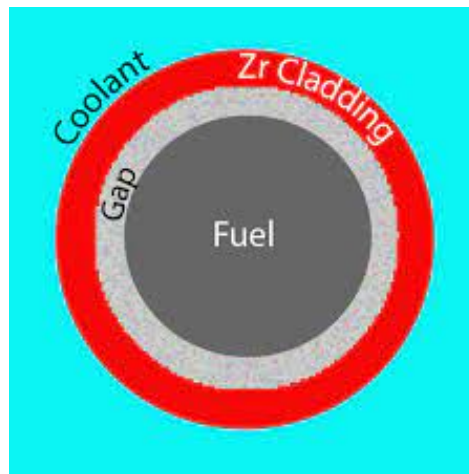


Figure 4.1: Schematic of a fuel rod

4.1 Coolant to clad interface

At the coolant-clad interface, the know temperature of the coolant T_{lb} is used to calculate the temperature at the cladding outer surface T_{co} using the equation,

$$T_{co} - T_{lb} \equiv \Delta T_{lb} = \frac{q''}{h} \quad (4.1)$$

where h is the heat transfer coefficient.

In light water reactors, the coolant is sub-cooled at the inlet to the reactor, which is the difference between the saturation temperature and the actual coolant bulk temperature $\Delta T_{sub} = T_f - T_{lb}$. So initially we will calculate the heat transfer from coolant to the clad in single-phase region using the equations:

- Prandlt number,

$$\text{Pr} = \frac{c_p \mu}{\lambda}$$

- Nusselt number (from the Dittus & Boelter correlation),

$$\text{Nu} = 0.023 \cdot \text{Re}^{0.8} \text{Pr}^{0.4}$$

- heat transfer coefficient,

$$h = \frac{\text{Nu} D_h}{\lambda}$$

For calculation in two-phase flow, we use the Chen correlation to calculate the heat transfer coefficient.

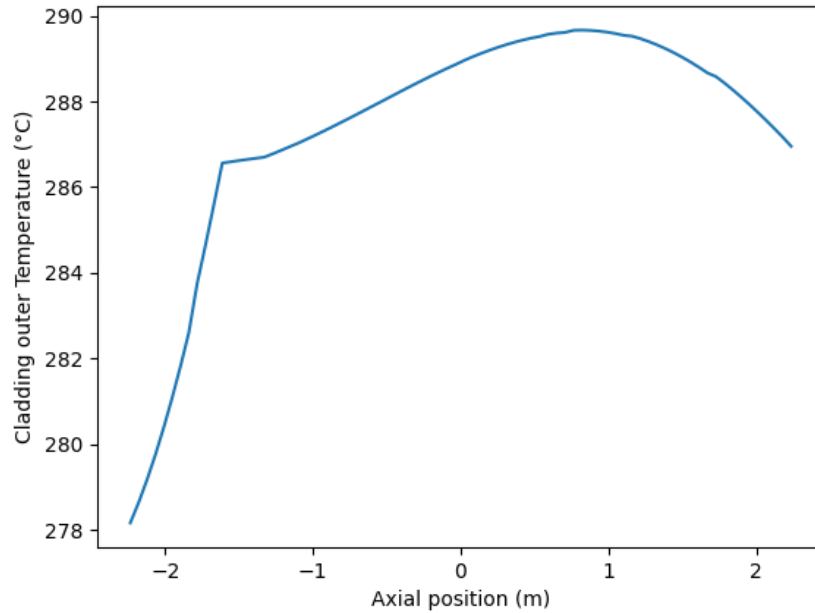


Figure 4.2: Axial distribution of outer cladding temperature

On figure 4.2, we can see that the maximum temperature on the outer surface of the cladding is reached above the middle of the core. This is understandable, as at this position the heating power is still quite high but the void fraction is getting higher, so the heat transfer from cladding to coolant is more difficult. Near the output, the void fraction is even higher and the transfer is more difficult but the heating power is also lower, so cladding temperature decreases.

After obtaining the temperature at the outer surface of the clad, we use the following expressions to calculate the temperature at the inner surface of the clad.

$$\Delta T_C = \frac{q''' r_{Fo}^2}{2\lambda_C} \ln \left(\frac{r_{Co}}{r_{Go}} \right) \quad (4.2)$$

where r_{Fo} is the radius of the fuel, r_{Co} is the thickness of the clad, r_{Go} is the thickness of the gas gap, and λ_C is the conductivity of the clad given by, $\lambda_C = 12.6 + 0.0118T$. The following figure show the axial distribution of temperature in the inner radius of the cladding that we obtained :

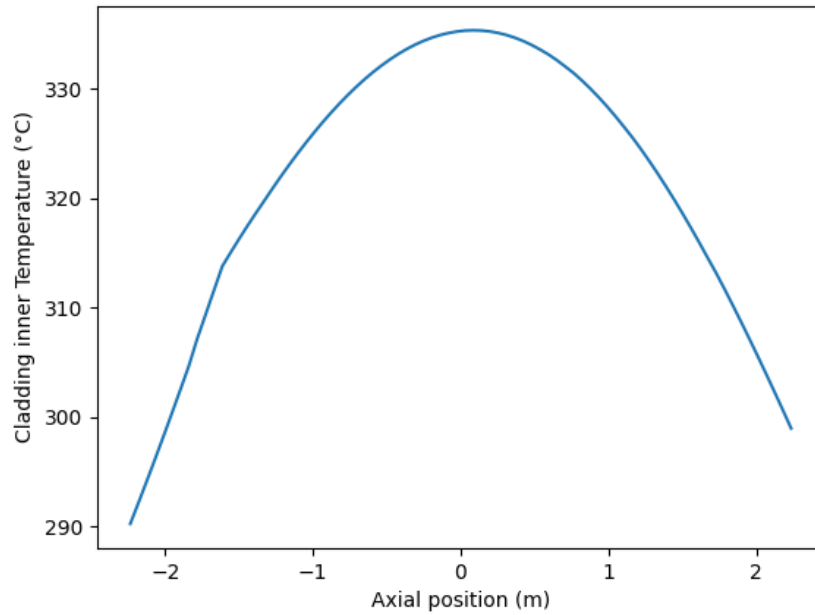


Figure 4.3: Axial distribution of inner cladding temperature

Using figures 4.2 and 4.3, we can see that the maximum temperature achieved in the cladding is reached on the inner radius of the cladding. This maximum temperature is 335.3°C and it is 2.32 m above the bottom of the core, i.e. a little bit above the middle of the core due to the influence of the coolant. This is far below the maximum allowed temperature of the the clad (given in Table 2) which means our clad will not melt in the core during operation at full power.

4.2 Gas to fuel interface

Using the temperature obtained at the inner surface of the clad T_{ci} which is also equal to the temperature of gas, T_{go} , at the outer radius of the Helium layer, we can easily calculate the temperature at the outer radius of the fuel (or inner radius of the gas), T_{fo} . Since the exact composition of the gas gap is unknown to us, we cannot formulate a correlation to use for the calculation of the thermal conductivity coefficient of gas λ_G . For the sake of this calculation, it is assumed that $\lambda_G = 0.378(70bar, 750^{\circ}C)$. With that assumption, we are now able to determine the temperature T_{fo} thanks to this equation :

$$\Delta T_G = \frac{q''' r_{Fo}^2}{2\lambda_G} \ln \left(\frac{r_{Go}}{r_{Fo}} \right) \quad (4.3)$$

The result that we obtained is visible in the figure 4.4 :

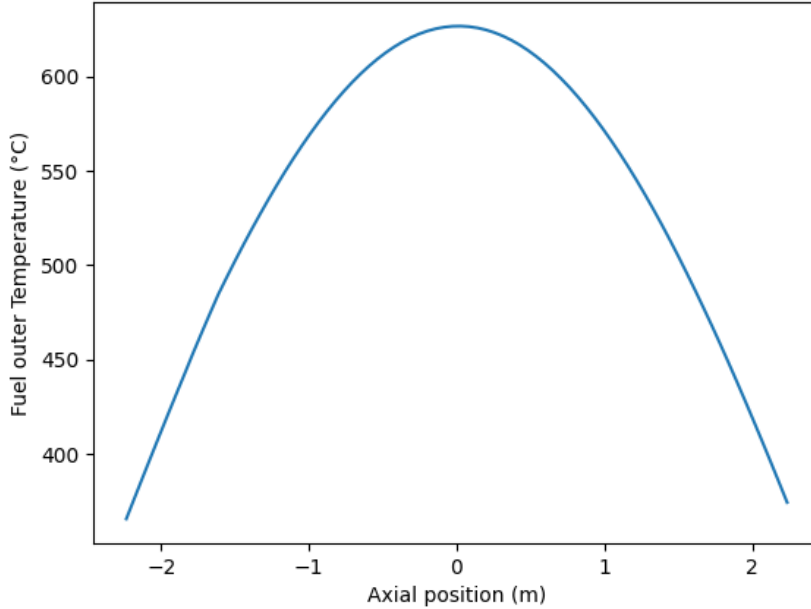


Figure 4.4: Axial distribution of the temperature on the outer radius of the fuel pellets

4.3 Fuel to fuel center interface

Now that we have calculated the temperature at the outer surface of the fuel pellets T_{fo} , we need to determine the temperature at the center of those fuel pellets. For that, we will use this equation :

$$\lambda_F \frac{dT_F}{dr} = -\frac{q'''(z)r}{2} \quad (4.4)$$

where λ_F is given by

$$\lambda_F(T) = \frac{100}{7.5408 + 17.692t + 3.6142t^2} + \frac{6400}{t^{5/2}} \exp \left(-\frac{16.35}{t} \right)$$

The temperature of the fuel is involved in the expression that we have for the thermal conductivity for UO_2 fuel pellets, and temperature changes a lot between the center and the outer surface of the fuel pellets, so in order to get a coherent result, we need to discretise equation 4.4. To do so, we decided to divide the fuel pellets into 100 cells of thickness l_{cell} .

By iteration, starting from the outer radius of the fuel pellets, we are now able to determine the temperature of a cell using the temperature of the previous calculated cell, moving progressively towards the center of the fuel pellets :

- Step 1:

$$\lambda_F(T_F(j)) \left(\frac{T_F(j) - T_F(j-1)}{l_{cell}} \right) = -\frac{q'''(z)j l_{cell}}{2} \quad \text{for } 1 < j < 100$$

- Step 2:

$$T(j-1) = T(j) + \frac{l_{cell}}{\lambda_F(T(j))} * \frac{q'''(z)j l_{cell}}{2}$$

By using this formula in a for loop for every axial cell, we were able to calculate the axial distribution of temperature at the center of the fuel pellets (figure 4.5), but also to determine the radial distribution of temperature inside the fuel pellets for every axial position in the core. For example, figure 4.6 shows the radial distribution of temperature inside the fuel pellets when z is the center of the rod, i.e. the point where the temperature of the fuel is maximal.

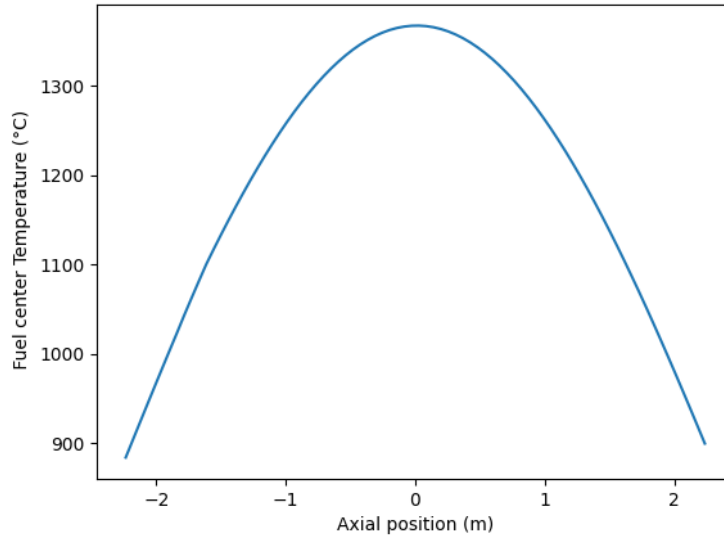


Figure 4.5: Axial temperature distribution at the center of the fuel

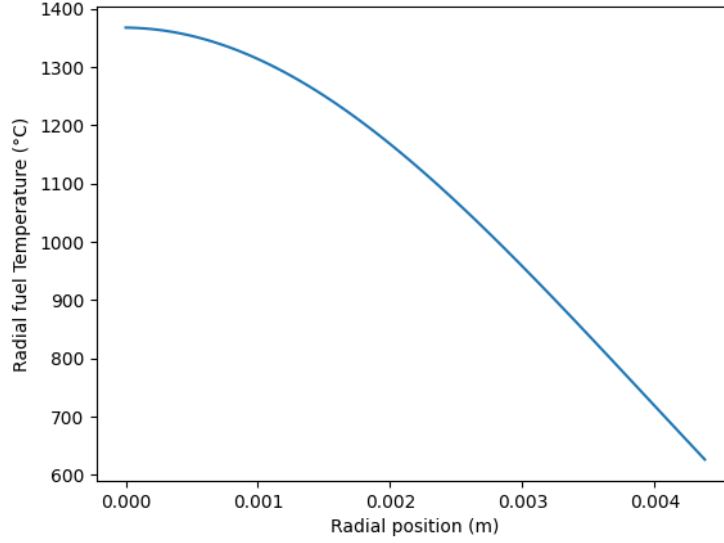


Figure 4.6: Radial temperature distribution inside a fuel pellet when $z = 2.235$ m

We see on figures 4.5 and 4.6 that the maximum temperature achieved at the center of the fuel pellet is 1388°C at 2.235 meters (at the center of the fuel rod). This is far below the maximum allowed temperature of the the fuel pellets (given in Table 2) which means our fuel will not melt in the core during operation at full power.

4.4 Radial distribution of temperature in gas layer and cladding

After calculating the temperature in every point of the fuel, we wanted to be able to get the temperature at any point of the whole fuel rod. To do so, we also divided radially the cladding and the gas into cells with the same length as the fuel cells. Then, we solved manually those two equations which allowed us to calculate respectively the temperature in the gas layer and the temperature in the cladding.

$$\frac{1}{r} \frac{d}{dr} \left(r \lambda_G \frac{dT_G(r)}{dr} \right) = 0$$

$$\frac{1}{r} \frac{d}{dr} \left(r \lambda_C \frac{dT_C(r)}{dr} \right) = 0$$

For the gas layer, the solution is found to be :

$$T_g(r) = (T_{go} - T_{fo}) * \frac{\ln\left(\frac{r}{r_{fo}}\right)}{\ln\left(\frac{r_{go}}{r_{fo}}\right)} + T_{fo} \quad (4.5)$$

where r_{Fo} is the outer fuel radius and r_{go} is the inner cladding radius (or outer gas radius).

For the cladding, the solution is found to be :

$$T_c(r) = (T_{co} - T_{go}) * \frac{\ln\left(\frac{r}{r_{go}}\right)}{\ln\left(\frac{r_{co}}{r_{go}}\right)} + T_{go} \quad (4.6)$$

where r_{co} is the outer cladding radius and r_{go} is the inner cladding radius.

Using those expressions, we were able to calculate the temperature in every point of the fuel rod. Figure (4.7) shows the radial distribution of the clad of thickness 0.66 mm at the axial location where maximum temperature is achieved. It is a quadratic curve, with maximum temperature of 335.3°C.

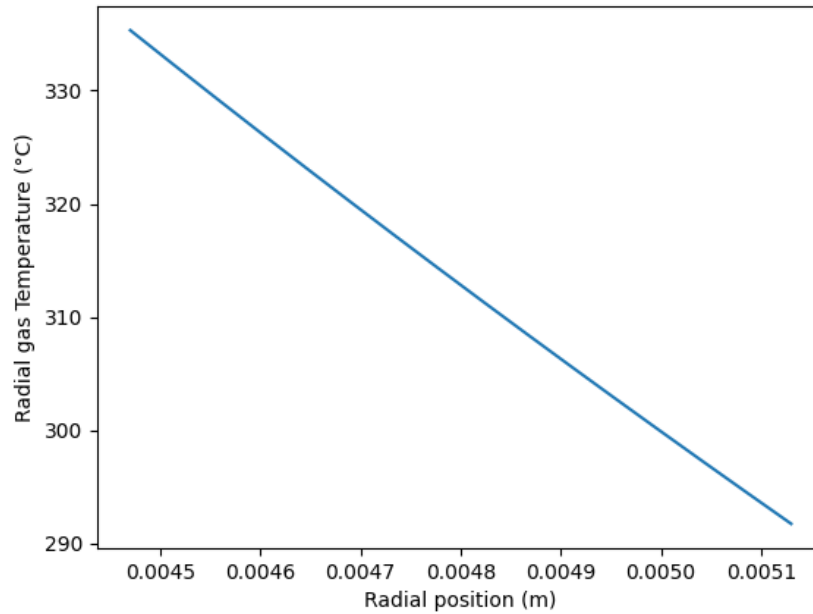


Figure 4.7: Radial distribution of the temperature inside the clad ($z = 2.32\text{m}$)

Figure (4.8) shows the radial distribution of temperature in the gas gap. It is a quadratic curve, with maximum temperature of 637°C.

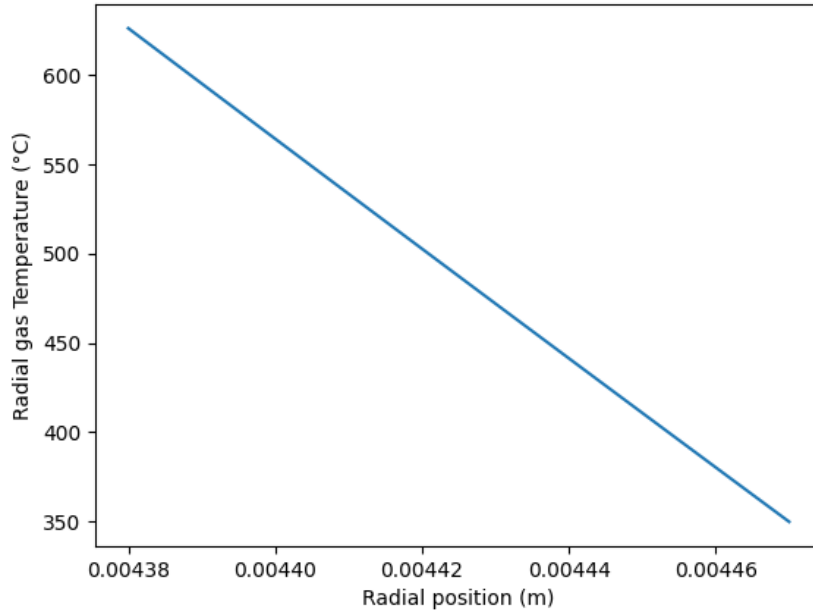


Figure 4.8: Radial distribution of temperature inside the gas gap ($z=2.235\text{m}$)

4.5 Conclusion and temperature field in the rod

All the graphs obtained for the whole calculation can be compiled to look like Figure 4.9. Some of the keen observations from the graph are listed below:

- The temperature does not change much in cladding, which is a good sign because thermal expansion in the clad would be dangerous.
- The gas gap is keeps for most of the heat from the fuel pellets and does not transfer them to the clad, filling its protecting role.
- The fuel pellets reach very high temperatures because that is where fission, which is a highly exothermic reaction, occurs.

Figure 4.9 shows the radial distribution of temperature in the whole rod, at $z = 2.235\text{m}$, which is the position corresponding to the middle of the rods, i.e. the point when maximum fuel temperature is reached.

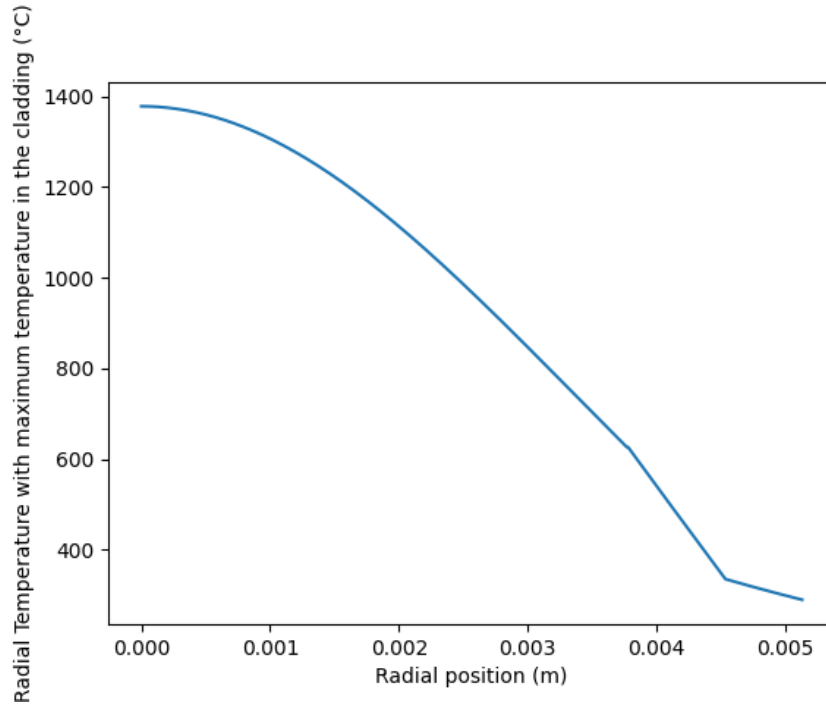


Figure 4.9: Radial temperature distribution in the whole rod

Finally, to get a better view of the temperature in the fuel rods, we used all the data that we had calculated to plot 2D temperature fields in the fuel rod. Figure 4.10 shows the temperature field inside the whole rod and figure 4.11 focuses on the cladding, revealing that the hottest spot is indeed in the inner surface of the cladding, a little bit above the middle of the fuel rod. (Warning : of course, we couldn't respect the proportions for length and thickness of the rod).

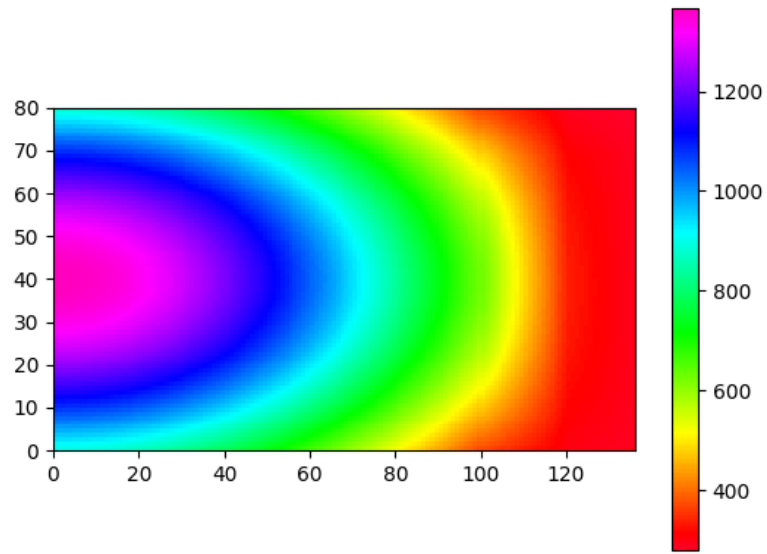


Figure 4.10: 2D temperature field in the whole fuel rod

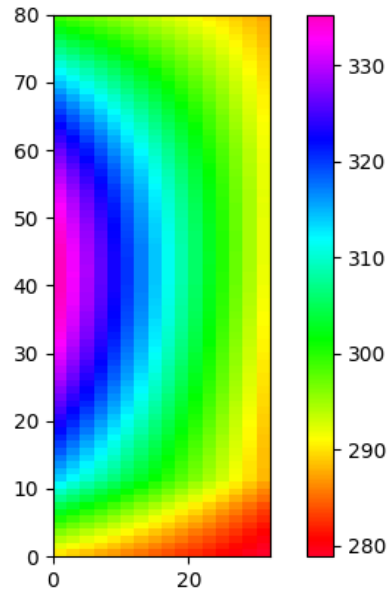


Figure 4.11: 2D temperature field in the cladding

A. Appendices

Parameters (Unit)	ABWR
Plant main Specification	
Electrical Output (MWe)	1356
Thermal Output (MWth)	3926
Number of Fuel Bundles	872
Core Lattice	C-Lattice
Reactor Pressure (MPa)	7.17
Feedwater Temp. (°C)	216
Main Steam Flow Rate (kg/s)	2122
RPV/RIN	
RPV Inner Diameter (m)	7.1
RPV Inner Height (m)	21.2
Number of Control Rods	205
CRGT Cross Section	Circular
RRS	
Rated Core Flow Rate (kg/s)	14500
Number of RIPs	10
Steam Separation System	
Number of Steam Separators	349
Number of Dryer Assemblies	6
MSL System	
Number of Main Steam Lines	4
Number of MSIVs	8
Number of SRVs	18
Nominal Capacity per SRV (kg/s)	110
CRD System	
Type of CRD	FMCRD

Features	ABWR	BWR/6
Recirculation	Vessel-mounted reactor internal pumps	Two external loop recirculation system with the jet pumps inside RPV
Control Rod Drives	Fine-motion control rod drives	Locking piston control rod drives
ECCS	3-division ECCS	2-division ECCS plus HPCS
Reactor Vessel	Extensive use of forged rings	Welded plate
Primary Containment	Advanced - compact, inerted	Mark III - large, low pressure, not inerted
Secondary Containment	Reactor Building	Shield, fuel, auxiliary and DG buildings
Control and Instrumentation	Digital, multiplexed, fiber optics, multiple channel	Analog, hard-wired, single channel
Control Room	Operator task-based	System-based
Severe Accident Mitigation	Inerting, drywell flooding containment venting	Not specifically addressed
Reactor Water Cleanup	2%, sealless pumps in cold leg	1%, pumps in hot leg
Offgas	Passive offgas with room-temperature charcoal	Active offgas with chilled charcoal filters

Table 3: Comparision of key features of ABWR and BWR/6

References

- [1] GE Hitachi Nuclear Energy. *The ABWR Plant General Description*. Hitachi, 2007.
- [2] Ken-ich Sato Masayoshi Matsuura Hirohide Oikawa, Takashi Sato. Abwr design and its evolution, safety system design. *GENES4*, 2003.
- [3] iaea. Advanced boiling water reactor (abwr). URL <https://aris.iaea.org/PDF/ABWR.pdf>.
- [4] Masaaki Tsubaki Hideo Soneda Katsumi Yamada, Satoko Tajima. Abwr design and its evolution. *GENES4*, 2003.
- [5] Heiping Li. Thermal hydraulics lecture slides. *KTH Royal Institute*, 2023.
- [6] Shigemi SUGINO Takaya SEKO, Daniel R. WILKINS and Jiro KANI. Modern technology applied in advanced bwr (abwr). *Journal of Nuclear Science and Technology*, pages 837–847, 2012.